Vector Field Topology of Time-Dependent Flows in a Steady Reference Frame

Irene Baeza Rojo and Tobias Günther
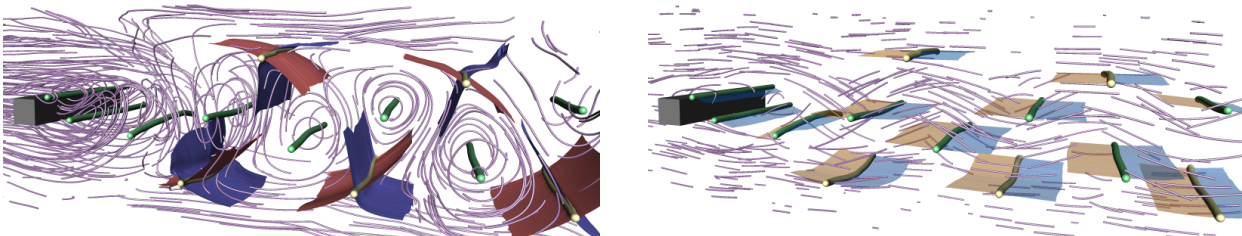

Fig. 1: Our method splits a vector field $\mathbf{v}(\mathbf{x},t)$ into two components: a steady flow $\mathbf{w}(\mathbf{x},t)$ and the ambient motion $\mathbf{f}(\mathbf{x},t)$. Feature curves such as vortex corelines (green), bifurcation lines (yellow) and their separating surfaces (blue and red in left image), can be extracted via streamline-oriented topology in $\mathbf{w}$, while the motion of these features (orange and blue in right image) is extracted as pathsurfaces in $\mathbf{f}$. As context, we show purple streamlines in $\mathbf{w}(\mathbf{x},t)$ (left) and purple pathlines in $\mathbf{v}(\mathbf{x},t)$ (right).

Abstract— The topological analysis of unsteady vector fields remains to this day one of the largest challenges in flow visualization. We build up on recent work on vortex extraction to define a time-dependent vector field topology for 2D and 3D flows. In our work, we split the vector field into two components: a vector field in which the flow becomes steady, and the remaining ambient flow that describes the motion of topological elements (such as sinks, sources and saddles) and feature curves (vortex corelines and bifurcation lines). To this end, we expand on recent local optimization approaches by modeling spatially-varying deformations through displacement transformations from continuum mechanics. We compare and discuss the relationships with existing local and integration-based topology extraction methods, showing for instance that separatrices seeded from saddles in the optimal frame align with the integration-based streamline vector field topology. In contrast to the streamline-based approach, our method gives a complete picture of the topology for every time slice, including the steps near the temporal domain boundaries. With our work it now becomes possible to extract topological information even when only few time slices are available. We demonstrate the method in several analytical and numerically-simulated flows and discuss practical aspects, limitations and opportunities for future work.

Index Terms— Scientific visualization, unsteady flow, vector field topology, reference frame optimization.

◆

---

1 INTRODUCTION

Feature extraction is a fundamental aspect of scientific visualization [14, 24, 30, 36]. Features may not only be relevant for an analysis task, they also provide entry points for visual exploration, data reduction and vector field design. A key problem of feature-based vector field analysis is the dependence of the flow vectors on the chosen frame of reference [11, 16, 32, 38]. Thus, recent feature definitions aimed for a reference frame invariance, making them invariant to certain types of motion, such as equal-speed translations [4, 27, 57] (known as Galilean invariance) or time-dependent rotations and translations [1, 19, 31] (known as objectivity). Recent work concentrated on the selection of an appropriate reference frame, for instance by a flow decomposition [2, 60, 62], an adjustment to features [4], machine learning [28] or a linear optimization [11, 16]. At present, reference frame optimizations have only been applied to vortex extraction [11, 13, 15, 16].

In this paper, we aim for an unsteady vector field topology based on reference frame optimizations, including topological elements (such as critical points and separatrices) and feature curves (such as vortex corelines and bifurcation lines). There are two types of approaches to unsteady vector field topology: local methods that observe only a single time slice, and integration-based methods. Local methods include the traditional streamline-oriented topology, which is known to not capture the behavior of pathlines [57]. Integration-based methods require the tracing of particles over time, e.g., the streakline-based topology [40] or flow map analysis [3]. Integration-based methods become inaccurate or even undefined near the temporal domain boundaries, since they have

to be able to observe particle behavior in the past and in the future.

Our local method is based on a suitable vector field decomposition [11] that splits a time-dependent vector field into two components: a vector field in which the flow becomes steady (which contains topological elements and features) and a second vector field that contains the ambient motion (describing where the elements move to). To formally model the motion of topological elements and features, we propose to use displacement fields from non-linear continuum mechanics [44], which naturally extend the concept of affine invariance [13] to more general types of spatially-varying motions. We show later that all currently existing classes of reference frame invariance appear as special cases. Since the decomposition is local in space and time, we can extract topological information everywhere in the domain, including near the temporal domain boundaries. In contrast to the global optimization method of Hadwiger et al. [16], our approach has a lower memory consumption, is an order of magnitude faster and has a smaller time partial residual. In the paper, we make the following contributions:

- We use a reference frame optimization to define topological elements and features in the frame in which the flow becomes steady.

- We generalize the affine-invariant reference frame optimization [13] to inhomogeneous displacement transformations in order to increase the accuracy, and compare our method with existing local and global optimizations [13, 16].

- We apply the ambient motion field to the space-time tracking of critical points (2D and 3D) and feature curves (vortex corelines and bifurcation lines in 3D) in optimal reference frames.

• *Irene Baeza Rojo and Tobias Günther are with the Computer Graphics Laboratory, ETH Zürich. E-mail: irene.baeza|tobias.guenther@inf.ethz.ch.*

- We compare our local optimization-based bifurcation line extraction with previous local and global approaches [33, 40] and discuss the relationship with FTLE.

Regarding topology, we concentrate on critical points and separatrices only. Our reference frame-based topology has potential to spur future work on other topological elements such as closed orbits, attachment/detachment points, boundary switches, saddle connectors and the various Hopf and fold bifurcations. Our formal characterization of motion provides the mathematical basis for an error quantification and a construction of ground truth examples.

2 BACKGROUND AND RELATED WORK

2.1 Reference Frames

2.1.1 Reference Frame Invariances for Feature Extraction

Formal feature definitions often depend on the frame of reference [11]. Since the motion between observer and feature is relative, reference frame invariance has a critical consequence: Being invariant to motions of the observer equals the invariance to motions of the feature. Thus, reference frame invariance enables us to successfully detect features that are moving. In increasing order of generality, the following reference frame invariances have been studied in fluid mechanics and scientific visualization. Galilean invariance is the invariance of a measure under equal-speed translations of the reference frame [57]. Rotation invariance is the invariance of a measure under equal-speed rotations of the reference frame around a known center of rotation [12]. Objectivity is the invariance of a measure under smooth rotations and translations of the reference frame. Objectivity has been studied in the context of vortex extraction [1, 6, 48] decades ago, and recently has seen a comeback initiated by the work of Haller et al. [19, 21, 22]. Finally, affine invariance is the invariance of a measure under smooth affine transformations of the reference frame [13]. From a continuum mechanics perspective, all above reference frame transformations have in common that they are *homogeneous deformations*, which means that their rotations, translations and affine transformations are assumed to be spatially constant. In the context of a local reference frame optimization, this means that the transformation is assumed to be constant within the local neighborhood, which might not necessarily hold.

In this paper, we extend these concepts to *inhomogeneous deformations*, i.e., spatially-varying deformations. For this, we explicitly model the spatial dependence in our derivation. Ultimately, all above reference frame invariances are contained as special cases.

2.1.2 Towards a Special Reference Frame

The path towards reference frame optimizations, i.e., the selection of a favorable reference frame, originated in the fluid mechanics literature on vortex dynamics. Lugt [32] and Robinson [38] similarly characterized a vortex by the observations of circular streamlines in a suitable reference frame. While Lugt requested a reference frame in which the flow is steady, Robinson suggested to search for a frame that follows the vortex center. In the 1970s, Lugt [32] already pointed out an important dilemma: A fluid is a continuum in which structures move non-uniformly. Therefore, it is not possible to find a single reference frame that moves with all structures at once. Perry and Chong [35] described this phenomenon at a jet in cross flow, in which vortices accelerate and become steady in different frames. It therefore became clear that a spatially-varying reference frame is necessary. For this reason, Günther et al. [11] introduced a linear optimization that searches at each grid point in a small local neighborhood for a rotation and translation in which the local neighborhood becomes steady. They extended the approach to affine transformations of the reference frame [13] and found applications in vortex extraction of finite-sized objects in fluids [15]. Hadwiger et al. [16] formulated the search as a global optimization, in which they restricted the individual observers to rigid motions. Such a global optimization allows for smoother solutions, but it is slow and has a high memory consumption. We argue that motion is determined by the local neighborhood and we thus use local optimizations. Recently, Kim and Günther [28] used deep learning to extract a steady reference frame from data with noise and resampling artifacts. This approach increases the numerical robustness, but it needs sufficient training data.

2.2 Steady Vector Field Topology

Steady vector field topology has been extensively researched [23, 30, 43, 56] and is formed by critical points, their invariant manifolds and the integral curves that connect the invariant manifolds [10]. Helman and Hesselink [25, 26] introduced first-order critical points, attachment and detachment points, and separatrices to the visualization community. A separatrix is a streamline starting from a saddle in one of its Jacobians' eigenvector directions. By now, many more elements complete the topological skeleton, such as boundary switch points [5], closed streamlines [51, 65] and boundary switch connectors [59]. Aside from first-order critical points, higher-order topological structures have been investigated [7, 42, 53]. Classic steady vector field topology has no reference frame invariance and is therefore not applicable to study the asymptotic behavior of pathlines in time-dependent flows [57]. Complementing the above topology, certain features such as vortex corelines and bifurcation lines likewise give order to 3D flows. However, these structures are not necessarily invariant manifolds.

2.3 Unsteady Vector Field Topology

Theisel et al. [52] distinguished between streamline-oriented and pathline-oriented topology. The latter observes the flow in the plane orthogonal to the pathline tangent in order to classify pathline sectors with attracting, repelling or saddle-like behavior. Haller [18] used finite-time Lyapunov exponents [46] (FTLE) as approximations of Lagrangian coherent structures (LCS). To identify hyperbolic trajectories, he proposed a hyperbolicity time measure [17] and introduced a finite-time counterpart that requires hyperbolic behavior over a time window [20]. Fuchs et al. [8] selected a reference frame in which both the acceleration of the original flow and the velocity in the transformed flow vanish. This approach is only Galilean invariant and they demonstrated that it does not solve the Beads problem [61]. Similarly, Bujack et al. [4] chose extrema in the determinant of the Jacobian as feature to pin the reference frame, which is Galilean invariant. Further, Fuchs et al. [8] introduced a local Galilean-invariant unsteadiness measure, which is the material derivative of the Jacobian. By Lagrangian smoothing, this measure searches for a Lagrangian frame that is as Galilean as possible. Based on the observation that FTLE converges to material structures at infinite integration duration [45], Germer et al. [9] computed flow maps over the full integration domain to obtain a variant of FTLE that is guaranteed to have no flux crossing. Sadlo and Weiskopf [40] suggested to calculate bifurcation lines [35] as intersections of forward and backward FTLE ridges, and replaced separatrices with generalized streaklines [63], released from the bifurcation line. The method has later been extended to 3D [54]. Their separatrices are limited to the locations that particles can reach in the finite time window, resulting in incomplete information near temporal domain boundaries. A local Galilean-invariant estimation of the 2D space-time bifurcation line was proposed by Machado et al. [33], based on the parallel vectors (PV) formulation [34] of the reduced velocity criterion [47]. The local PV extraction is followed by an iterative tangent alignment to obtain an approximate bifurcation line that is a pathline. As a counterpart to closed streamlines, Wilde et al. [64] extracted recirculation surfaces. We also refer to the surveys of Pobitzer et al. [36] and Heine et al. [23].

To study topological elements and features, a number of flow decompositions have been proposed. Similar to Wiebel et al. [62], Bhatia et al. [2] removed a harmonic flow component, using a Helmholtz-Hodge decomposition. A split of the the flow into a steady flow and an ambient motion has been mentioned by Günther and Theisel [11] in the context of vortex extraction, but has not yet been applied to extract elements of a topological skeleton or to extract bifurcation lines.

3 OVERVIEW OF TIME-DEPENDENT TOPOLOGY

In this paper, we build a time-dependent vector field topology on top of a reference frame optimization. This includes the definition of topological elements, their extraction and their tracking over time. This section gives an overview of the approach and summarizes key findings.
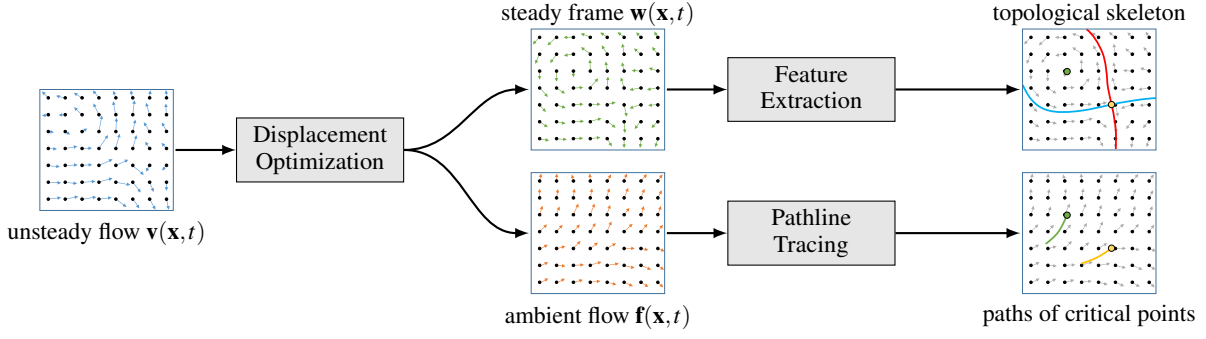
Fig. 2: Overview of our unsteady vector field topology extraction. First, a reference frame optimization is performed to split the input flow $\mathbf{v}(\mathbf{x},t)$ into a flow in a steady reference frame $\mathbf{w}(\mathbf{x},t)$ and the ambient motion $\mathbf{f}(\mathbf{x},t)$. From the slices of $\mathbf{w}(\mathbf{x},t)$, we extract the classic streamline-based vector field topology and features, while the paths of critical points are given as pathlines in the ambient flow $\mathbf{f}(\mathbf{x},t)$.

3.1 Decomposition into Features and Ambient Motion

Our approach is fundamentally based on the vector field decomposition of a time-dependent vector field $\mathbf{v}(\mathbf{x},t)$ into the flow in its steady reference frame $\mathbf{w}(\mathbf{x},t)$ and the ambient motion $\mathbf{f}(\mathbf{x},t)$:

$$\underbrace{\mathbf{v}(\mathbf{x},t)}_{\text{input field}} = \underbrace{\mathbf{w}(\mathbf{x},t)}_{\text{steady frame}} + \underbrace{\mathbf{f}(\mathbf{x},t)}_{\text{ambient motion}} \quad (1)$$

The decomposition is illustrated in Fig. 2, showing that topological elements such as critical points and separatrices can be extracted from the steady frame $\mathbf{w}(\mathbf{x},t)$ and that the paths of critical points appear as pathlines in the ambient flow $\mathbf{f}(\mathbf{x},t)$.

3.2 Key Observations

Our approach has the following properties:

- We extract reference frames locally in space-time faster and with lower memory consumption than global approaches [16].

- Unsteady topology is defined in all time slices, in contrast to the integration-based streakline topology [40,54].

- Separatrices in optimal frames (single slice with time partials) align with integration-based streakline topology [40] separatrices.

- The integration of bifurcation lines in $\mathbf{f}(\mathbf{x},t)$ is far more stable than in $\mathbf{v}(\mathbf{x},t)$.

- Saddles in the optimal frame are located at FTLE ridge intersections for a long integration duration.

- Our topology is naturally reference frame invariant, up to the degrees of freedom in the optimization, including objectivity, affine invariance and more.

- The Lagrangian coherence of our topological elements can be measured by the length of the feature tracks in time.

In the following section, we introduce a generalization of the recent affine-invariant reference frame extraction [13], which we use to compute our vector field decomposition. Note that any other reference frame optimization could be used that splits the flow into a steady and an ambient motion component. We later compare our novel approach with existing methods, showing that our approach is more accurate.

4 VECTOR FIELDS IN VARYING FRAMES

4.1 Reference Frame Transformations

Previous local reference frame optimizations [11, 13] assumed the ambient motion to be constant within a certain neighborhood. The following section introduces our novel general spatially and temporally-varying reference frame transformation from a rather practical point of view without proofs. The derivations for this section can be found in full detail in the additional material (Sections 2–4).

4.1.1 Displacement Transformation of a Vector Field

To describe a spatially and temporally-varying reference frame transformation, continuum mechanics gives us two approaches [44]: domain deformations [12, 29] and displacement transformations. In principal, both are very similar, though the latter allows us to derive a vector field decomposition more easily. We introduce a displacement vector field $\mathbf{F}(\mathbf{x},t)$ that moves a space-time point $(\mathbf{x},t)$ to its destination $(\mathbf{x}^*,t)$ via[1]

$$\mathbf{x}^* = \mathbf{x} + \mathbf{F}(\mathbf{x},t) \quad (2)$$

Formally, $\mathbf{F}$ is a diffeomorphism, i.e., it is an invertible transformation that maps between the two differentiable spaces. In other words, it is bijective and does not produce folds or overlaps in space. A given vector field $\mathbf{v}(\mathbf{x},t)$ is transformed to $\mathbf{v}^*(\mathbf{x}^*,t)$ via:

$$\mathbf{v}^*(\mathbf{x}^*,t) = [\mathbf{I} + \nabla \mathbf{F}(\mathbf{x},t)] \cdot \mathbf{v}(\mathbf{x},t) + \mathbf{F}_t(\mathbf{x},t) \quad (3)$$

Note that Galilean, objectivity and affine invariance are included as special cases, which is shown in the additional material (Sect. 3).

4.1.2 Derivatives of Displacement Transformations

After application of a displacement transformation, the acceleration $\mathbf{a}^*$, Jacobian $\mathbf{J}^*$ and time partial $\mathbf{v}_t^*$ of the resulting vector field are:

$$\mathbf{a}^*(\mathbf{x}^*,t) = [\mathbf{I} + \nabla \mathbf{F}(\mathbf{x},t)] \cdot \mathbf{a}(\mathbf{x},t) + \frac{D\nabla \mathbf{F}(\mathbf{x},t)}{Dt} \cdot \mathbf{v}(\mathbf{x},t) + \frac{D\mathbf{F}_t(\mathbf{x},t)}{Dt} \quad (4)$$

$$\mathbf{J}^*(\mathbf{x}^*,t) = \left[\mathbf{J}(\mathbf{x},t) + \nabla \frac{D\mathbf{F}(\mathbf{x},t)}{Dt} \right] \cdot [\mathbf{I} + \nabla \mathbf{F}(\mathbf{x},t)]^{-1} \quad (5)$$

$$\mathbf{v}_t^*(\mathbf{x}^*,t) = \mathbf{v}_t(\mathbf{x},t) + \nabla \mathbf{F}(\mathbf{x},t) \cdot \mathbf{v}_t(\mathbf{x},t) + \frac{D\mathbf{F}_t(\mathbf{x},t)}{Dt} \quad (6)$$

$$- \left[\mathbf{J}(\mathbf{x},t) + \nabla \frac{D\mathbf{F}(\mathbf{x},t)}{Dt} \right] \cdot [\mathbf{I} + \nabla \mathbf{F}(\mathbf{x},t)]^{-1} \cdot \mathbf{F}_t(\mathbf{x},t)$$

We refer to Section 4 of the additional material for the derivations.

4.2 Computation of Steady Reference Frame

4.2.1 Problem Statement

Our goal is to minimize the time partial derivative that is obtained after a reference frame transformation, i.e., $\mathbf{v}_t^*(\mathbf{x}^*,t)$ in Eq. (6):

$$\|\mathbf{v}_t^*(\mathbf{x}^*,t)\|^2 \to \min \quad (7)$$

Eq. (6) shows us that $\mathbf{v}_t^*(\mathbf{x}^*,t)$ only depends on spatial and temporal derivatives of $\mathbf{F}(\mathbf{x},t)$ – not on the value of $\mathbf{F}(\mathbf{x},t)$ itself. Thus, where a coordinate $\mathbf{x}$ is displaced to at time t is a degree of freedom. We choose to not move the features, keeping them at their physical location in the space-time domain. Thus, the displacement at observation time t_0 is:

$$\mathbf{F}(\mathbf{x},t)|_{t=t_0} = \mathbf{0} . \quad (8)$$

---
[1]For simplicity, we assume that the transformation does not shift time.

Together with Eq. (2), this simplifies the computation greatly, since:

$$\mathbf{x}^*_{|t=t_0} = \mathbf{x} \tag{9}$$

$$\nabla \mathbf{F}(\mathbf{x},t)_{|t=t_0} = \nabla(\nabla \mathbf{F}(\mathbf{x},t))_{|t=t_0} = \mathbf{0} \tag{10}$$

Thus, Eqs. (3), (5) and (6) simplify to:

$$\mathbf{v}^*(\mathbf{x},t)_{|t=t_0} = \mathbf{v}(\mathbf{x},t) + \mathbf{F}_t(\mathbf{x},t) \tag{11}$$

$$\mathbf{J}^*(\mathbf{x},t)_{|t=t_0} = \mathbf{J}(\mathbf{x},t) + \nabla \mathbf{F}_t(\mathbf{x},t) \tag{12}$$

$$\mathbf{v}^*_t(\mathbf{x},t)_{|t=t_0} = \mathbf{v}_t(\mathbf{x},t) + \nabla \mathbf{F}_t(\mathbf{x},t) \cdot \mathbf{v}(\mathbf{x},t) - \mathbf{J}(\mathbf{x},t) \cdot \mathbf{F}_t(\mathbf{x},t) + \mathbf{G}(\mathbf{x},t) \tag{13}$$

with the vector field $\mathbf{G}(\mathbf{x},t)$ being:

$$\mathbf{G}(\mathbf{x},t) = \mathbf{F}_{tt}(\mathbf{x},t) - \nabla \mathbf{F}_t(\mathbf{x},t) \cdot \mathbf{F}_t(\mathbf{x},t) \tag{14}$$

Eq. (13) shows that $\mathbf{F}_t$ and $\mathbf{G}$ are needed to obtain the optimal displacement. In fact, Eq. (13) is *linear* in these two unknowns. Since we have more unknowns than equations, we use a regularization. We minimize the time partial $\mathbf{v}^*_t(\mathbf{x},t)_{|t=t_0}$ within a small neighborhood region U:

$$\min_{\mathbf{F}_t,\mathbf{G}} \int_U \|\mathbf{v}^*_t(\mathbf{x},t)_{|t=t_0}\|^2 \, dV \tag{15}$$

which enforces smoothness in the unknown fields $\mathbf{F}_t$ and $\mathbf{G}$. In the following, we derive a *local* linear optimization to calculate these two unknowns. The key difference to previous methods [13] is that we allow for spatially-varying $\mathbf{F}_t$ and $\mathbf{G}$ within neighborhood U.

4.2.2 Spatial Variation by Taylor Expansion

In order to adapt to spatial variations of $\mathbf{F}_t$ and $\mathbf{G}$ within the neighborhood U, we spatially discretize these derivatives by a component-wise multi-variate m-th order Taylor expansion around the observation point $\mathbf{x}_0$, i.e., the center of neighborhood region U:

$$\mathbf{F}_t(\mathbf{x},t) = \sum_{m=0}^{\infty} \frac{1}{m!} \nabla^m \mathbf{F}_t(\mathbf{x}_0,t) \cdot (\mathbf{x} - \mathbf{x}_0)^m \tag{16}$$

$$\nabla \mathbf{F}_t(\mathbf{x},t) = \sum_{m=1}^{\infty} \frac{1}{(m-1)!} \nabla^m \mathbf{F}_t(\mathbf{x}_0,t) \cdot (\mathbf{x} - \mathbf{x}_0)^{m-1} \tag{17}$$

$$\mathbf{G}(\mathbf{x},t) = \sum_{m=0}^{\infty} \frac{1}{m!} \nabla^m \mathbf{G}(\mathbf{x}_0,t) \cdot (\mathbf{x} - \mathbf{x}_0)^m \tag{18}$$

with $\nabla^m \mathbf{F}_t(\mathbf{x}_0,t)$ and $\nabla^m \mathbf{G}(\mathbf{x}_0,t)$ being symmetric tensors of order m. For notational convenience, we treat the tensor entries as vectors. This way, these three terms can have any arbitrary polynomial degree in $\mathbf{x}$ and are themselves linear in their tensor coefficients. Later in Section 7.7, we show results for other approximations than Taylor, namely Fourier approximations and Chebyshev approximations.

W.l.o.g., we shift the coordinates such that the center of the neighborhood region U is located at $\mathbf{x}_0 = \mathbf{0}$. To simplify the notation we set $\mathbf{F}_t^{(m)} = \nabla^m \mathbf{F}_t(\mathbf{x}_0,t)$ and $\mathbf{G}^{(m)} = \nabla^m \mathbf{G}(\mathbf{x}_0,t)$. By inserting Eqs. (16)–(18) into Eq. (13), we get time partial $\mathbf{v}^*_t(\mathbf{x},t)_{|t=t_0}$ in Taylor expansion:

$$\mathbf{v}^*_t(\mathbf{x},t)_{|t=t_0} = \mathbf{v}_t(\mathbf{x},t)$$
$$+ \sum_{m=0}^{\infty} \left[\mathbf{F}_t^{(m)} \cdot \frac{\mathbf{x}^{m-1}}{(m-1)!} \cdot \mathbf{v}(\mathbf{x},t) - \mathbf{J}(\mathbf{x},t) \cdot \mathbf{F}_t^{(m)} \cdot \frac{\mathbf{x}^m}{m!} \right]$$
$$+ \sum_{m=0}^{\infty} \mathbf{G}^{(m)} \cdot \frac{\mathbf{x}^m}{m!} \tag{19}$$

In the next section, we discuss how Eq. (19) is minimized.

4.2.3 Linear Least Squares Minimization

Note that $\mathbf{v}^*_t(\mathbf{x},t)_{|t=t_0}$ is *linear* in the unknowns $\mathbf{F}_t^{(i)}$ and $\mathbf{G}^{(i)}$ for $i \in \{0,\ldots,m\}$. Setting $\mathbf{v}^*_t(\mathbf{x},t)_{|t=t_0} = \mathbf{0}$, Eq. (19) can thus be arranged to:

$$\mathbf{M}(\mathbf{x},t) \cdot \mathbf{p}(\mathbf{x},t) = -\mathbf{v}_t(\mathbf{x},t) \tag{20}$$

with the system matrix $\mathbf{M}$ containing a series of squared matrices

$$\mathbf{M} = \left(\underbrace{\mathbf{F}_{00},\mathbf{G}_{00}}_{\text{zero-order}}, \underbrace{\mathbf{F}_{10},\mathbf{G}_{10},\mathbf{F}_{01},\mathbf{G}_{01}}_{\text{first-order}}, \underbrace{\mathbf{F}_{20},\mathbf{G}_{20},\mathbf{F}_{11},\mathbf{G}_{11},\mathbf{F}_{02},\mathbf{G}_{02}}_{\text{second-order}}, \ldots \right) \tag{21}$$

and the corresponding vector of unknowns $\mathbf{p}$, containing the coefficients $\mathbf{f}_{ij}$ and $\mathbf{g}_{ij}$ of the Taylor expansion of $\mathbf{F}_t$ and $\mathbf{G}$, respectively:

$$\mathbf{p} = \left(\underbrace{\mathbf{f}_{00},\mathbf{g}_{00}}_{\text{zero-order}}, \underbrace{\mathbf{f}_{10},\mathbf{g}_{10},\mathbf{f}_{01},\mathbf{g}_{01}}_{\text{first-order}}, \underbrace{\mathbf{f}_{20},\mathbf{g}_{20},\mathbf{f}_{11},\mathbf{g}_{11},\mathbf{f}_{02},\mathbf{g}_{02}}_{\text{second-order terms}}, \ldots \right)^{\mathrm{T}} \tag{22}$$

Here, $\mathbf{M}$ and $\mathbf{p}$ are shown for the 2D case. The 3D case can be found in the additional material. In the 2D case, $\mathbf{M}$ is a $2 \times (m^2 + 6m + 4)$ matrix and $\mathbf{p}$ is a $(m^2 + 6m + 4) \times 1$ vector. In the 3D case, $\mathbf{M}$ is a $3 \times (m^3 + 6m^2 + 11m + 6)$ matrix and $\mathbf{p}$ is a $(m^3 + 6m^2 + 11m + 6) \times 1$ vector. The construction of $\mathbf{M}$ and $\mathbf{p}$ is described in the additional material for 2D and 3D (Sect. 5). The quadratic energy in Eq. (15) is minimized by solving the linear least squares problem:

$$\widehat{\mathbf{M}}\mathbf{p} = \widehat{\mathbf{y}} \tag{23}$$

$$\widehat{\mathbf{M}} = \int_U \mathbf{M}^{\mathrm{T}}\mathbf{M} \, dV \qquad \widehat{\mathbf{y}} = -\int_U \mathbf{M}^{\mathrm{T}}\mathbf{v}_t \, dV \tag{24}$$

Let $\bar{\mathbf{p}}$ be the optimal $\mathbf{p}$, minimizing Eq. (23). The optimal $\bar{\mathbf{p}}$ contains the coefficients of the Taylor expansion of $\mathbf{F}_t(\mathbf{x},t)$ in Eq. (16). Thus, after optimization, $\mathbf{F}_t(\mathbf{x},t)$ is evaluated and inserted into Eqs. (11)–(12) to compute $\mathbf{v}^*(\mathbf{x},t)_{|t=t_0}$ and $\mathbf{J}^*(\mathbf{x},t)_{|t=t_0}$ in the optimal reference frame.

5 UNSTEADY TOPOLOGY IN STEADY FRAMES

In the optimal reference frame, the vector field becomes steady, which allows us to study the time-dependent flow $\mathbf{v}(\mathbf{x},t)$ by means of the traditional steady vector field topology [10,25,26].

Flow in Steady Frame. The previous section showed how to calculate the vector field $\mathbf{v}^*(\mathbf{x},t)_{|t=t_0}$, which is the input field $\mathbf{v}(\mathbf{x},t)$ in the local optimal frame. For notational convenience, we will call this vector field $\mathbf{w}(\mathbf{x},t)$ in the remainder of the paper:

$$\mathbf{w}(\mathbf{x},t) = \mathbf{v}^*(\mathbf{x},t)_{|t=t_0} \tag{25}$$

$$\nabla\mathbf{w}(\mathbf{x},t) = \mathbf{J}^*(\mathbf{x},t)_{|t=t_0} \tag{26}$$

$$\mathbf{w}_t(\mathbf{x},t) = \mathbf{v}^*_t(\mathbf{x},t)_{|t=t_0} \tag{27}$$

It is important to note that the spatial and temporal derivatives of $\mathbf{w}(\mathbf{x},t)$ cannot be computed by finite differences, since each point might be in a different reference frame. Instead, Eqs. (26)–(27) have to be used.

Ambient Motion. The ambient motion $\mathbf{f}(\mathbf{x},t)$ can be calculated by rearranging Eq. (1) to $\mathbf{f}(\mathbf{x},t) = \mathbf{v}(\mathbf{x},t) - \mathbf{w}(\mathbf{x},t)$. With Eq. (3), we get:

$$\mathbf{f}(\mathbf{x},t) = -\frac{D\mathbf{F}(\mathbf{x},t)}{Dt} = -\nabla\mathbf{F}(\mathbf{x},t) \cdot \mathbf{v}(\mathbf{x},t) - \mathbf{F}_t(\mathbf{x},t) \tag{28}$$

For the *local*[2] decomposition in Eq. (11), we get $\mathbf{f}(\mathbf{x},t)_{t=t_0} = -\mathbf{F}_t(\mathbf{x},t)$.

5.1 Topological Elements and Feature Curves

In this paper, we focus mainly on two topological elements, namely critical points and separatrices. In addition, we extract bifurcation lines, their separating surfaces and vortex corelines.

Critical Points. The foundation of the traditional topological skeleton are *critical points*[3], also called stationary points or singularities. We follow the first-order characterization of Helman and Hesselink [25,26].

---

[2]Local means that $\overline{\text{Eqs. (8)–(10)}}$ apply.

[3]The term critical point is usually coined for minima, maxima and saddles in scalar fields. In the visualization literature [25], it is also used for vector fields.
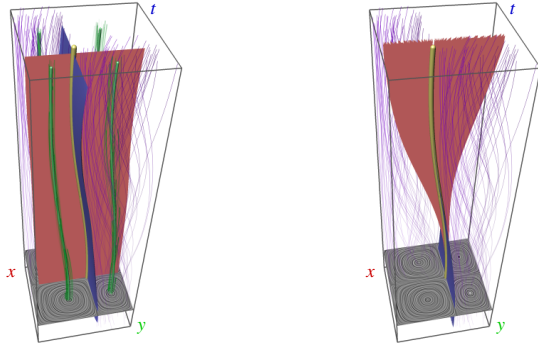
(a) Our displacement optimization   (b) Sadlo and Weiskopf [40]

Fig. 3: Difference between the separatrices obtained with our local method and the streakline-based approach [40]. The method of Sadlo and Weiskopf [40] misses parts of the separation surface near the temporal domain boundary. While they studied bifurcations (yellow curve), we also extract vortex corelines (green curves). LIC slices show the flow in the optimal reference frame and pathlines (purple) were released in two sectors, showing that no particles cross the separatrices.

Separatrices. Separatrices segment the flow into areas of coherent behavior. In steady vector fields, and also in our optimal steady reference frame, they can be calculated by releasing particle trajectories from saddles. By connecting the curves over time t, separating surfaces are obtained in space-time. Fig. 3 shows a space-time visualization of the separatrices extracted with our method and with the streakline-based topology of Sadlo and Weiskopf [40]. Our separatrices can be traced in each time slice separately using streamlines in $\mathbf{w}(\mathbf{x},t)$, whereas the streakline-based method releases pathlines forward and backward in time in $\mathbf{v}(\mathbf{x},t)$. Due to the limited time domain, their method cannot construct the full separating surfaces near the temporal domain boundaries. In 3D, we have three eigenvalues, two of them having the same sign. The two corresponding eigenvectors span a plane in which a streamsurface can be released. In the direction of the eigenvector with the oppositely signed eigenvalue, a streamline can be released in $\mathbf{w}$.

Vortex Corelines and Bifurcation Lines. First-order vortex corelines and bifurcation lines are defined in 2D space-time and 3D using the parallel vectors operator [34] via $\mathbf{w} \parallel (\nabla \mathbf{w})\mathbf{w}$, with constraints on the eigenvalues of the Jacobian. For vortex corelines, the eigenvalues must be complex [41]. For a bifurcation line, the determinant measured in the plane orthogonal to the flow must be negative [33]. Note that these feature curves are not formally part of the topological skeleton, because they might not be invariant manifolds if they end in the domain.

5.2 Properties

Next, we emphasize two important properties of our decomposition.

Paths of 2D Critical Points are Pathlines. It turns out that every critical line $\mathbf{x}_c(t)$ in the space-time domain of $\mathbf{w}(\mathbf{x},t)$, such as a bifurcation line or a vortex coreline, is a pathline in both $\mathbf{v}(\mathbf{x},t)$ and $\mathbf{f}(\mathbf{x},t)$. This is because these structures are critical points in the time slices of $\mathbf{w}$, i.e., $\mathbf{w}(\mathbf{x}_c(t),t) = \mathbf{0}$, and thus with $\mathbf{v} = \mathbf{w} + \mathbf{f}$ in Eq. (1) their ambient motion is identical to the underlying flow:

$$\mathbf{w}(\mathbf{x}_c(t),t) = \mathbf{0} \ \Rightarrow \ \mathbf{v}(\mathbf{x}_c(t),t) = \mathbf{f}(\mathbf{x}_c(t),t) \qquad (29)$$

This property is in alignment with the usual request that vortex corelines are tangential to the flow [14, 57]. A theoretical consequence is that critical paths can be tracked in space-time as pathlines in the input unsteady flow $\mathbf{v}(\mathbf{x},t)$ or in the ambient motion $\mathbf{f}(\mathbf{x},t)$ in Eq. (28). Note, however, that integration in $\mathbf{v}(\mathbf{x},t)$ can be extremely unstable, for instance, when tracing along a bifurcation line, since a tiny numerical error would lead to an exponential push off the bifurcation line. The field $\mathbf{f}(\mathbf{x},t)$, on the other hand, follows the feature on and in the vicinity of the critical point and thus integration of bifurcation lines is more stable, see the additional material for an example (Sect. 8). Stable feature flow fields [58] could further reduce integration errors.

Generalization of Feature Flow Fields. Our ambient motion $\mathbf{f}(\mathbf{x},t)$ in Eq. (28) can be seen as generalization of the feature flow field [50] to arbitrary displacement transformations, since the traditional feature flow field $\mathbf{f}(\mathbf{x},t) = -\mathbf{J}^{-1}\mathbf{v}_t$ [13] appears as special case as the solution to Eq. (6) for Galilean displacement transformations, i.e., for $\nabla \mathbf{F}_t = \mathbf{0}$ and $\mathbf{F}_{tt} = \mathbf{0}$. This connection inspired our naming of the ambient motion field as $\mathbf{f}(\mathbf{x},t)$.

6 IMPLEMENTATION

Building up on the open source implementation of Günther et al. [13], we share a C++ demo implementation for the 2D case in the additional material. As in [11], the integration of the system matrix in Eq. (24) within neighborhood U can be done by summed-area tables (SAT). This speeds up the calculation, but it requires additional memory. In 2D, the system matrix size grows quadratic in the Taylor order. In 3D, it grows cubic, see the additional material. The SAT therefore grows very quickly in size, as shown in Section 7.8. Note, however, that our method is local and it is thus possible to compute only partial SATs for blocks of the data set, and to process the domain block-by-block. While our implementation processes the time slices sequentially and is partially OpenMP parallelized, there is still room for improvements. At each grid point, we solved the local linear system with a Householder QR decomposition with full-pivoting. We extracted critical points by recursive subdivision [10] and computed vortex corelines and bifurcation lines in 2D space-time and in 3D with the parallel vectors operator [34].

7 RESULTS

7.1 Construction of Flow with Ground Truth Topology

In order to test our numerical optimization, we need a method to construct an analytical vector field where we know the ground truth positions of its topological elements. For this, we take the inverse approach: Given a steady vector field $\mathbf{v}^*(\mathbf{x}^*,t)$, we transform it *backward* with a known displacement transformation, resulting in a time-dependent vector field $\mathbf{v}(\mathbf{x},t)$. A backward displacement transformation of a vector field $\mathbf{v}^*(\mathbf{x}^*,t)$ is done by rearranging Eq. (3) to:

$$\mathbf{v}(\mathbf{x},t) = [\mathbf{I} + \nabla \mathbf{F}(\mathbf{x},t)]^{-1} (\mathbf{v}^*(\mathbf{x}+\mathbf{F}(\mathbf{x},t),t) - \mathbf{F}_t(\mathbf{x},t)) \qquad (30)$$

This formulation allows us to sample the time-dependent test vector field $\mathbf{v}(\mathbf{x},t)$ onto a space-time grid $(\mathbf{x},t)$. We can now use our optimization to recover the forward transformation $\mathbf{F}(\mathbf{x},t)$ from $\mathbf{v}(\mathbf{x},t)$, which takes us back to the steady vector field $\mathbf{v}^*(\mathbf{x}^*,t)$.

Modified Double Gyre. Inspired from Shadden's Double Gyre [46], we construct a MODIFIED DOUBLE GYRE for our analytical ground truth topology. Shadden defined a steady vector field as co-gradient of a stream function. By deforming the stream function, the resulting time-dependent co-gradient vector field is divergence-free. However, this construction approach cannot control the location of features, such as vortex corelines and bifurcation lines. Instead, we apply a displacement transformation using Eq. (30) to compute our unsteady vector field $\mathbf{v}(\mathbf{x},t)$. With Eq. (29), we know that critical lines in the optimal frame $\mathbf{w}(\mathbf{x},t)$ are pathlines of $\mathbf{v}(\mathbf{x},t)$. In the domain $[0,2] \times [-1,1]$, vortex corelines pass through $(x,y,t) = (1\pm 0.5, \pm 0.5, 0)$, and a bifurcation line passes through $(x,y,t) = (1,0,0)$, see Fig. 3. The derivation of this construction is shown in the additional material (Sect. 7).

7.2 Comparison with Previous Reference Frames

7.2.1 Comparison of Residuals on Ground Truth

Using our vector field with its ground truth transformation, we now compare the energy residuals, i.e., the transformed time partials, of previous methods with our approach for varying approximation orders. Fig. 4a depicts the input vector field and Fig. 4b displays the ground truth in the optimal frame. The two vortices are visible and there is no cross-flow across the separating structure in the middle. The generic objective method [11] in Fig. 4c and our zero-order displacement optimization in Fig. 4e result in similar time partial residuals. The residuals $\mathbf{w}_t(\mathbf{x},t)$ are color-coded with a heat color map. The global optimization of Hadwiger et al. [16] in Fig. 4d performed slightly better, followed

(a) Input flow $\mathbf{v}(\mathbf{x},t)$ (b) Ground truth $\mathbf{w}(\mathbf{x},t)$

$\varepsilon = 4.01 \times 10^{-2}$ timing= 0.86 sec $\varepsilon = 3.32 \times 10^{-2}$ timing= 1.9 min

(c) Objectivity [11]   (d) Hadwiger et al. [16]

$\varepsilon = 4.35 \times 10^{-2}$ timing= 0.92 sec $\varepsilon = 2.73 \times 10^{-2}$ timing= 1.85 sec

(e) constant displacement ($m=0$)   (f) Affine invariance [13] ($m=1$)

$\varepsilon = 2.95 \times 10^{-3}$ timing= 4.96 sec $\varepsilon = 7.98 \times 10^{-4}$ timing= 11.8 sec

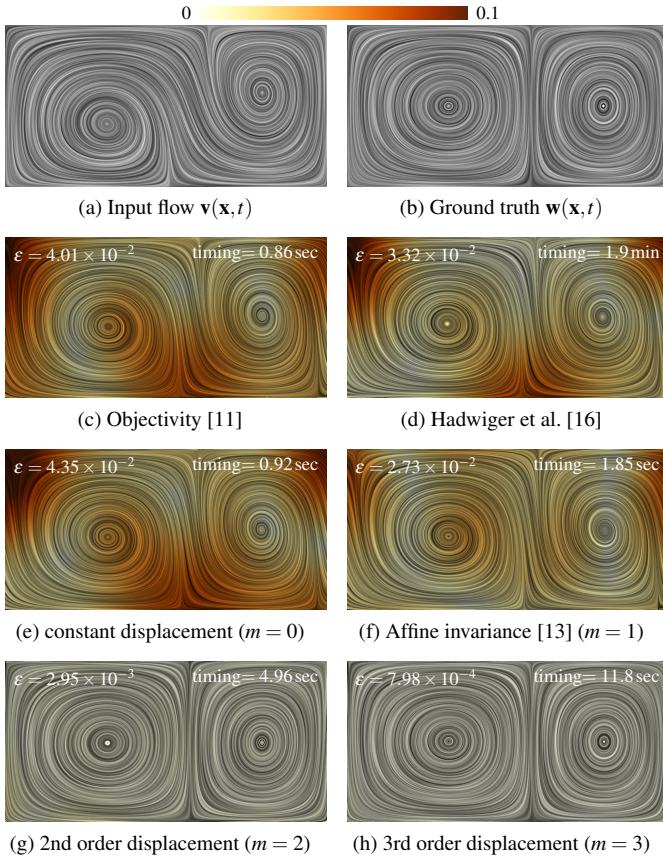(g) 2nd order displacement ($m=2$)   (h) 3rd order displacement ($m=3$)

Fig. 4: Comparison of the optimization methods at $t = \pi/3$ in the MODIFIED DOUBLE GYRE with time partial residual mapped to color. The RMSE time partial residual is denoted as ε. Note that the low-order methods exhibit a flow across the vertical boundary in the middle.

by the affine-invariant method [13] in Fig. 4f, which is equivalent to our first-order displacement optimization. All above four methods give very similar results with a RMSE time partial residual in the order of 10^{-2}, still showing cross-flow across the separatrix. Significant improvements are made with our second-order displacement optimization in Fig. 4g, pushing the residual down to 10^{-3}. The results become indistinguishable from the ground truth when using our third-order displacement optimization in Fig. 4h, which has an error in the order of 10^{-4}. Aside from the improved accuracy, our local third-order method is an order of magnitude faster than the global approach [16].

7.2.2 Comparison at Vortex Coreline Extraction

In Fig. 5, we use the BOUSSINESQ flow to compute vortex corelines and compare our third-order optimization with previous reference frame optimizations. An approach to test the correctness of a vortex coreline in 2D space-time is to release pathlines from the coreline in order to see if the particles stay close to the coreline and swirl around it. The method of Hadwiger et al. [16] in Fig. 5a resulted in the smoothest reference frame, but missed weak corelines compared to the affine-invariant method [13] in Fig. 5b and our third-order displacement optimization in Fig. 5c. Overall, all methods give fairly good results. If a smooth solution is preferred, the approach of Hadwiger remains a solid choice, while our displacement optimization is favorable when precision is key.

7.3 Comparison with Bifurcation Line Extractors

Next, we study another important feature curve: bifurcation lines. For those, there are two main competitors: the integration-based intersection of FTLE ridges [40] and the local parallel vectors approach [33].

7.3.1 Comparison with FTLE Ridge Intersection

The intersection of forward and backward FTLE ridges has two problems. First, it requires an integration duration to be set and, as pointed

(a) Approximate killing fields of Hadwiger et al. [16], default parameters   timing= 33.5 min

(b) Affine-invarince by Günther and Theisel [13], $N = 41^2$ timing= 11.2 sec

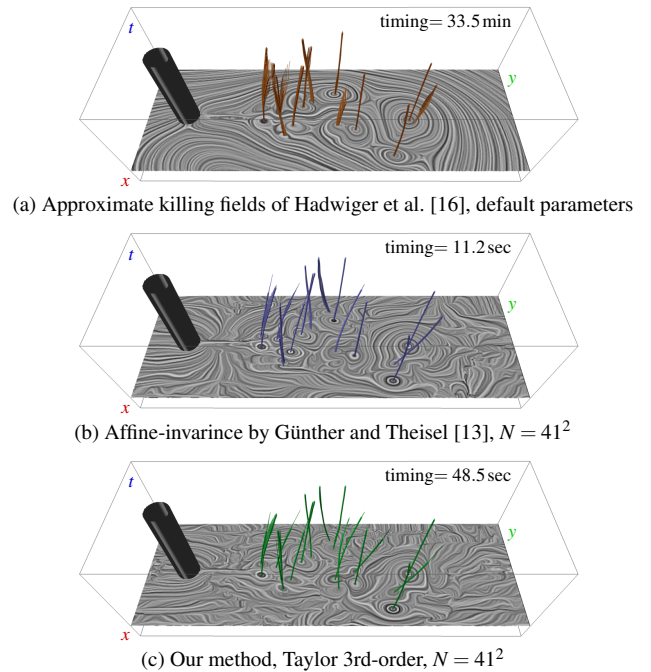(c) Our method, Taylor 3rd-order, $N = 41^2$ timing= 48.5 sec

Fig. 5: Comparison of our displacement optimization with previous local [13] and global [16] approaches in space-time in the BOUSSINESQ flow. To confirm the correctness of the vortex corelines, particles are released on them and are integrated forward and backward. If a vortex coreline is a pathline, particles stay close and swirl around it. Our method has the lowest error and finds more vortices than the other two.

out by Shadden [46], FTLE ridges converge to material lines in the limit of infinite integration duration. Therefore, integrating too short leads to wrong locations. Second, integrating too long results in false positives, since intersections also occur in other locations. Fig. 6 shows line integral convolutions of our optimal steady reference frame with an overlay of the FTLE ridges in forward (red) and backward (blue) direction for varying integration durations. For a short integration duration, the ridges are fuzzy and slightly off. For a longer duration, the intersection is more precise, but false-positives appear above and below the vortices. This experiment shows that saddles in our local reference frame correspond to integration-based FTLE ridge intersections. Sect. 8 of the additional material contains results for the PIPED CYLINDER.

7.3.2 Comparison with Local and Integration-based Extractors

Next, we compare the local bifurcation line extractor of Machado et al. [33] and the FTLE ridge intersection of Sadlo and Weiskopf [40] with our displacement optimization. In Fig. 7a, our result for a second-order displacement optimization is shown for the MODIFIED DOUBLE GYRE. The ground truth bifurcation line is always shown in yellow. From the three methods, our green coreline is the closest. The LIC slice in the background shows our optimal reference frame, clearly revealing the saddle. The intersection of FTLE ridges in Fig. 7b is slightly off, since the integration duration of $\tau = 3$ was too short. For longer integration durations, further ridges appear very quickly. Finally, the method of Machado et al. is shown in Fig. 7c, which is clearly off, showing the acceleration field in the background. In 2D unsteady flows, critical points in the acceleration correspond to the PV locations in space-time [14]. Machado et al. [33] applied an iterative refinement to align the extracted line with a pathline, but there is no guarantee that this will converge to the correct solution. To make PV extraction a valid option, we first need to move into the steady reference frame.

7.4 Comparison with Streakline-based Separatrices

Up until now, releasing generalized streaklines from a bifurcation line [40] was the only option for the extraction of separatrices, which requires particle integration through time. Instead, we extract separatrices directly in a single time slice of our optimal reference frame.
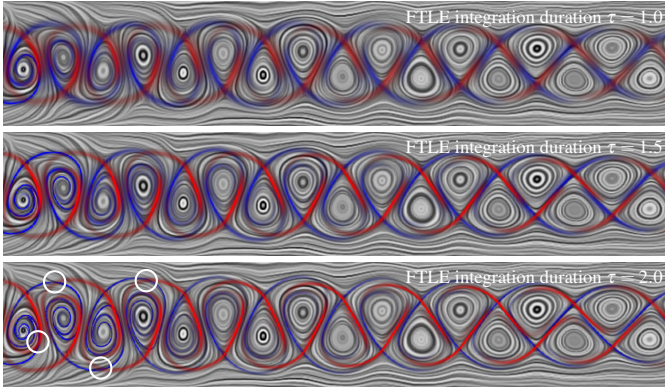
Fig. 6: Comparison of our third-order reference frame optimization (LIC shows optimal frame) with forward (red) and backward FTLE (blue) for varying integration duration τ. In this experiment, we used a neighborhood of $N = 31^2$ voxels for our method. Note the false-positive FTLE ridge intersections (highlighted with white circles).
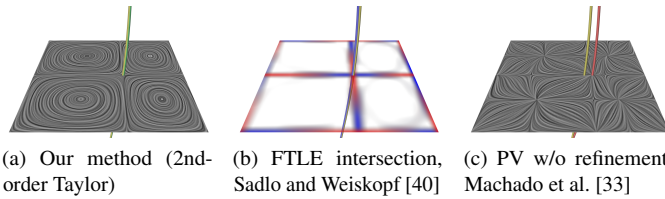

(a) Our method (2nd-order Taylor) (b) FTLE intersection, Sadlo and Weiskopf [40] (c) PV w/o refinement, Machado et al. [33]

Fig. 7: Comparison of local and integration-based bifurcation line extractors. The ground truth line is shown in yellow. The slices show the scalar or vector field, in which the lines are extracted. Note that our local approach finds the ground truth coreline best, closely followed by the FTLE intersection, which depends on the integration length.

7.4.1 Separatrices Among Deforming Centers

Our first example is based on the four centers flow [12], but uses a different transformation by transforming the co-gradient of a stream function with a spatially-varying displacement transformation that not only rotates the domain but also has structures moving at different speed based on their location. The latter is a transformation that the affine-invariant method cannot fit too. The vector field and its transformation can be found in the additional material (Sect. 7). In Fig. 8, we show separatrices obtained from individual slices in the affine-invariant reference frame, in our displacement optimized reference frames and with the streakline-based topology approach. Since the latter integrates pathlines, separatrices are only known where particles visit, giving an incomplete picture near the temporal domain boundary where only one direction (attracting or repelling) can be traced. This example demonstrates that our streamline-based separatrices in the optimal frame coincide with the streakline-based topology, but now we can compute the topology per time slice and thus trace the separatrices throughout the entire domain, not depending on particle integration through time. To experimentally confirm the correctness of the separatrices, we released particles in two sectors of the domain and display their pathlines (purple) to observe that they do not cross our separatrices in space-time.

7.4.2 Separatrices in Compressible Flow

Next, we study the separatrices in a compressible vector field containing sinks, sources and saddles. For this, a vector field is constructed such that the separatrices are curved lines by using a steady vector field and a spiraling transformation. Details on the construction can be found in the additional material (Sect. 7). Fig. 9 displays the extracted separatrices in space-time. An indicator for the correctness of a bifurcation line is that the four separatrices, that were released in close proximity from the bifurcation line, result in four different separating surfaces. The streakline-based topology was also seeded from our bifurcation line, showing that four different surfaces appear. As before, our method gives the complete separating surfaces, connecting the saddles with
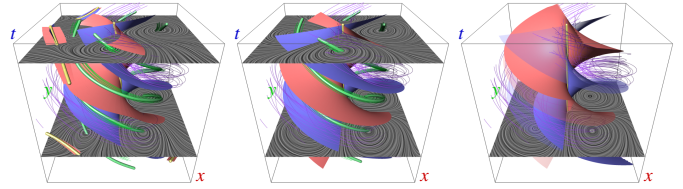
(a) Affine invariance [13] (b) Our 3rd-order method (c) Streakline topo. [40]

Fig. 8: Comparisons of affine invariance, our third-order displacement transformation, and the streakline-based topology of Sadlo et al. [40] with bifurcation lines (yellow) and vortex corelines (green). The affine-invariant approach cannot fit the transformation perfectly and thus finds artificial bifurcation lines from which separatrices do not grow as from a real saddle. Purple lines show pathlines, which do not cross our separatrices. In the last image, our displacement-optimized separatrices are visualized transparently, showing that our method finds the complete surfaces. The LIC visualizes the flow in the respective optimal frame.
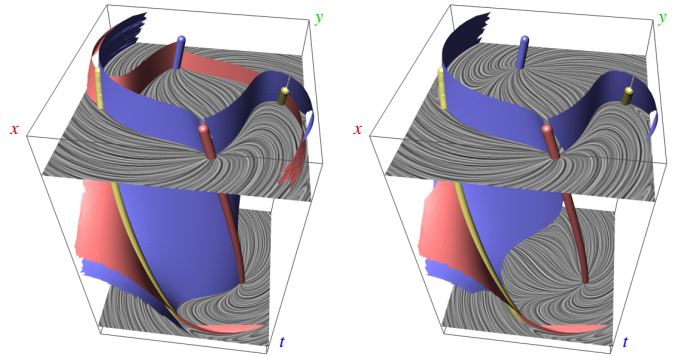
(a) Our method, 3rd-order optimization (b) Streakline-based separatrices [40]

Fig. 9: Space-time visualization of a flow containing sinks and sources. The streakline-based separatrices cannot compute the separatrices everywhere. Our method, on the other hand, connects the saddles with the sink and source in each time slice.

both sink and source in all time slices.

7.5 Unsteadiness due to Changing Magnitude

Based on Vatistas [55] experimentally-obtained velocity profile, we study an analytic vortex where tangential velocity of the vortex changes over time. The vector field is defined in the additional material (Sect. 7). The optimal frame $\mathbf{w}(\mathbf{x},t)$ and the ambient motion $\mathbf{f}(\mathbf{x},t)$ are shown in Fig. 10 for $t = 5$. Our optimization finds a reference frame in which the flow becomes steady, thereby turning the critical point into a spiraling sink. Thus, when vortex structures change the tangential velocity, we can expect a steady frame that is no longer divergence-free.

7.6 Applications in 2D and 3D

2D Cylinder Flow. Fig. 11 shows vortex corelines (green), bifurcation lines (yellow) and the repelling (red) and attracting (blue) separating surfaces in the CYLINDER 2D flow. The vortex corelines and bifurcation lines were computed with the parallel vectors operator [34] using our 3rd-order displacement optimization. The streakline-based method finds only small portions of the separatrices, since particles leave the domain early. Our local method extends these surfaces by tracing them in space only. The left and right part of the image show wrinkles in the separating surfaces due to temporal instability of the corelines. Below, a single time slice with longer separatices is shown. We can see that separatrices do not meet everywhere in the domain. This is perfectly consistent with the FTLE ridges in Fig. 6 and is due to a temporal change that is not purely governed by the motion, cf. Section 7.5. We refer to the video for an animation, showing that particle motion is indeed governed by the separatrices.
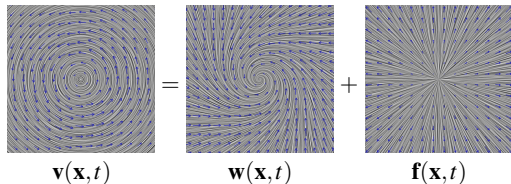
Fig. 10: If the magnitude of a vector field **v** changes in time, the optimal frame **w** contains a sink/source. The ambient motion **f** points out/in.

Streakline-based separatrices [40]

Our method, 3rd-order optimization

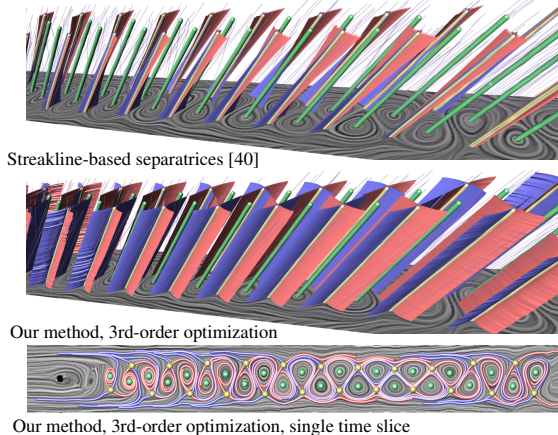Our method, 3rd-order optimization, single time slice

Fig. 11: Vortex corelines (green) and bifurcation lines (yellow) with separating surfaces (red and blue) in the space-time domain of the CYLINDER 2D flow. As context, pathlines were released (purple).

2D Piped Cylinder. Our next simulation contains two cylinder flows around two corners at Reynolds number $Re = 160$. Initially, a vortex street forms behind an obstacle, which then flows around two corners. Behind each corner, a standing vortex forms. The latter one blocks half of the flow to the second obstacle, creating a one-sided vortex street. A space-time illustration of our third-order results is given in Fig. 12 (left), containing the paths of vortices (green) and separatrices (yellow) with their separating surfaces over time. In a side view (right), many pathlines are shown that rotate around the vortex corelines and are attracted and repelled by the separating surfaces, showing that they indeed act as material boundaries as expected. We refer to the additional material for a visualization of the topology in a 2D time slice and its comparison with forward and backward FTLE.

3D Square Cylinder Flow. Fig. 1 gives an example of the extracted topology in the SQUARE CYLINDER flow at $t = 80$, showing vortex corelines (green) and bifurcation lines (yellow). The left image depicts the flow in the steady frame, including separating surfaces (red and blue), whereas the right image shows the paths of the feature curves. Note that again the separatrices emanating from different bifurcation lines do not perfectly meet, which is likely to be caused by the dissipation of the vortices, i.e., the unsteadiness of this flow is not only determined by motion, cf. Section 7.5. Sect. 8 of the additional material contains ambient motion surfaces with feature curves extracted at a later time step.

3D Half Cylinder. Fig. 13 shows a more complicated 3D example of a fluid simulation generated using Gerris flow solver [37], where the obstacle is a half cylinder and the Reynolds number has been increased to $Re = 320$ to add more turbulence to the simulation. The vortex street still forms, but the corelines and bifurcation lines are bent, making the extraction more challenging. While vortex corelines are still captured well, we can see that one bifurcation line is not passing through its saddle critical points in $\mathbf{w}(\mathbf{x},t)$. This shows that the extraction is still numerically challenging, which opens opportunities for future research.

3D Turbulent Rotating Mixer. In Sect. 8 of the additional material, another example of an even more turbulent flow can be seen. In turbulent flows, a large number of topological structures appears, which limits the applicability of topology-based methods.
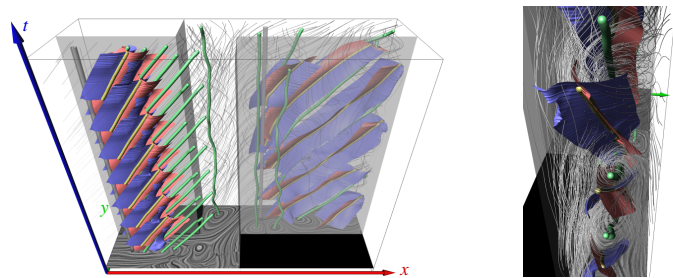

Fig. 12: Space-time visualization of the PIPED CYLINDER. Left: separating surfaces, bifurcation lines (yellow) and vortex corelines (green) are extracted in the two vortex streets. The second street is one-sided. The two standing vortices trap the flow behind the corners. Right: in a close-up with many pathlines, vortical motion around the vortex corelines and the ordering behavior of separatrices is visible.
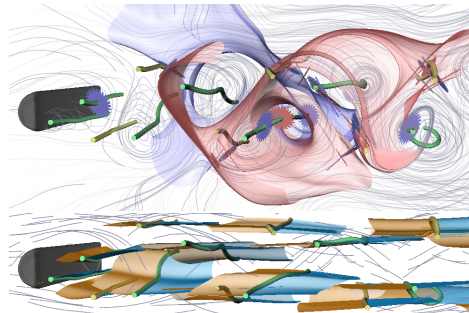

Fig. 13: Example in the HALF CYLINDER flow. Top: critical points, vortex corelines (green), bifurcation lines (yellow), and the complex separatring surfaces of one bifurcation line (red/blue). Bottom: the ambient motion $\mathbf{f}(\mathbf{x},t)$ of the feature curves and pathlines in $\mathbf{v}(\mathbf{x},t)$.

7.7 Parameter Studies

Neighborhood Region U. Fig. 14 shows the time partial residual for varying neighborhood sizes U in the CYLINDER 2D flow. In the wake of the obstacle, the residual is the largest and increases with growing U. This aside, the location of critical points is stable everywhere in the domain for all U. Generally, the neighborhood size must be large enough to contain more voxels than unknowns in the linear system. Due to the Taylor expansion, the movement is allowed to be spatially varying inside the neighborhood. Note that, the more degrees of freedom added, the larger the U must be to obtain a full rank system.

Continuous Basis Representations. In Section 4.2.2, we decided to describe the spatial variation of the reference frame transformation parameters $\mathbf{F}_t$ and $\mathbf{G}$ within the neighborhood U in monomial basis using a Taylor expansion. We experimented with other basis representations, such as the Chebyshev basis (as an alternative polynomial basis representation) and the Fourier basis. The results and derivation of the linear system for those cases can be found in the additional material, Sect. 6. Note that a zero-order approximation ($m = 0$) is identical in all cases and that Taylor and Chebyshev have an identical first-order approximation ($m = 1$). We empirically found that the Taylor representation worked best for us and we thus use it in the paper.

7.8 Performance

We measured the performance on an Intel i7-6700K CPU with 4 GHz and with 32 GB main memory. The timings and the memory consumption of the SAT are reported in Table 1 for varying Taylor approximation orders on all data sets, together with the grid resolutions and the neighborhood sizes used throughout the paper. We measured the timings for the entire space-time volume in 2D and for a single time slice in 3D. For 2D flows, a third-order Taylor approximation ($m = 3$) is efficient (about 73 seconds for 100 time slices) and the memory consumption for the SAT is around 100–800 MB in our examples. In 3D, we recommend the second-order approximation ($m = 2$) when using a single SAT for the entire domain.

Data Set	Affine / Taylor 1st		Taylor 2nd		Taylor 3rd		Grid	Time Slices	U
	time (sec)	SAT (MB)	time (sec)	SAT (MB)	time (sec)	SAT (MB)			
MOD. DOUBLE GYRE, Fig. 3	1.83	4.8	5.04	18.7	11.9	51.2	128×64	64	128^2
DEFORMING CENTERS, Fig. 8	2.62	9.8	6.37	37.5	16.4	102.5	128×128	64	128^2
SINK-SOURCE-SADDLE, Fig. 9	2.51	9.8	6.46	37.5	16.0	102.5	128×128	64	128^2
CHANGING MAGNITUDE, Fig. 10	2.53	9.8	5.96	37.5	15.1	102.5	128×128	64	128^2
CYLINDER 2D, Fig. 6	19.1	30.5	38.4	117.2	72.8	320.3	640×80	100	31^2
BOUSSINESQ, Fig. 5	11.2	76.2	24.4	293.0	48.5	800.8	600×200	31	41^2
PIPED CYL., Fig. 12	19.9	40.2	45.1	154.5	99.6	422.3	450×150	100	81^2
SQUARE CYL., Fig. 1	5.41	450	29.3	2,745	228.0	10,890	$192 \times 64 \times 16$	1	41^3
MIXER, Fig. 6 (Add. Mat)	2.52	600	12.0	3,660	581.9	14,520	$64 \times 64 \times 64$	1	41^3
HALF CYL., Fig. 13	5.69	797.4	29.5	3015.7	264.8	11964.1	$120 \times 90 \times 20$	1	51^3

Table 1: Timings and memory consumption for varying Taylor approximation orders (m) in all data sets. The timings are measured in seconds and the memory consumption is reported in MB. In 2D, the computation time for the entire space-time domain is listed, whereas in 3D the timings for a single time slice are reported. The grid resolution, number of time slices in the timings and the neighborhood size U are listed for all data sets.
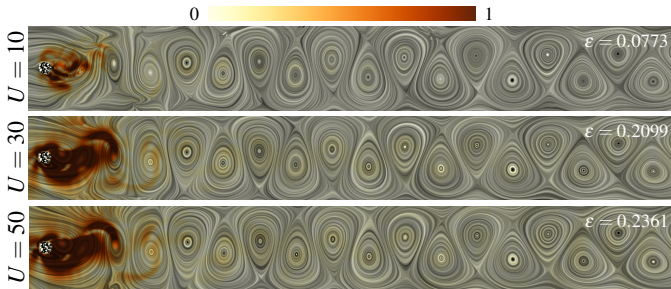

Fig. 14: Reference frame optimizations with 3rd-order Taylor approximation for varying neighborhood sizes U. The color map encodes the magnitude of the time partial residual $\|\mathbf{w}_t\|$. The number ε lists the RMSE of the time partial across the entire domain.

7.9 Discussion

Lagrangian Coherent Structures. The term Lagrangian coherent structure (LCS) implies that a feature is persistent in time. Several feature definitions have been designed based on this concept [21]. However, they require an integration duration to be set over which the features are calculated. This parameter is not necessarily easy to tune, as we have seen earlier at the bifurcation line extraction via FTLE ridge intersection. A temporal accumulation of a measure over a fixed time window is unaware of the actual existence of the feature. For instance, when a feature disappears mid-way, we cannot pin down at which time the event happened. Using our local method, we can extract space-time paths and their Lagrangian coherence can simply be measured by their length in the time dimension.

Uniqueness of Solution. Our optimization reduces to a linear least squares minimization, which has a unique minimum. Since our Taylor approximation has several unknowns, we need at least as many sample points in the local neighborhood U to obtain a full-rank system.

Consistency with Steady Case. When a steady flow is given as input $\mathbf{v}$, our method is equivalent to the well-established streamline-based topology [25, 26]. This follows from Eq. (24), since for a vanishing time partial $\mathbf{v}_t$, the right hand side $\hat{\mathbf{y}}$ of the linear system becomes zero, allowing the trivial solution $\mathbf{p} = \mathbf{0}$. This in turn leads to a zero ambient motion $\mathbf{f} = \mathbf{0}$, and hence our method does not change the input, giving $\mathbf{v} = \mathbf{w}$ as desired.

Physical Properties in Reference Frames. We should carefully choose which physical properties we want to observe in a steady reference frame. For some effects, such as vorticity or saddle-like behavior, we want to factor out the ambient motion. The change in volume (i.e., divergence) is a combined effect that depends on the ambient motion and it is likely to be better observed in the original frame. Certainly, we could search for decompositions that preserve divergence, such as objective transformations, but this might be unnecessarily restricting when we are looking for a steady frame.

Tracking of Parallel Vectors Solutions. Theisel et al. [49] derived a vector field to track parallel vectors solutions. Note that our ambient motion field is not a generalization of this and it should not be. The PV characterization of vortex corelines and bifurcation lines implies certain shape assumptions (first-order implies zero curvature, second-order implies zero torsion [39]). This might give different solutions and the ambient motion field should not favor any one of them. Instead, we identify motion directions via reference frames. If the shape assumption of the parallel vectors feature is fulfilled, and if the feature is passively advected with the flow, then our ambient motion field will track it.

Limitations. We used inhomogeneous deformations to describe ambient motion and used a linear optimization to compute them. Since our method is local and applied per time slice, the resulting topological elements are not guaranteed to be temporally coherent, which can be seen in the video. In the future, we would like to investigate strategies to enhance the temporal coherence. A practical concern is that the linear optimization requires good estimates of spatial and temporal derivatives. Especially in the light of large-scale simulations, we think that future simulation codes should write time partials to disk if they store only few time steps. The dependence on good temporal derivative estimations is studied in the additional material (Sect. 8) with another experiment.

8 CONCLUSION

We introduced a general reference frame optimization that searches for a spatially-varying displacement field such that a vector field evolving under this displacement transformation becomes steady. This gave rise to a vector field decomposition into a flow in the steady reference frame and the remaining ambient motion. While the steady frame is used to extract elements of the standard steady vector field topology as well as vortex corelines and bifurcation lines, the ambient motion describes the motion of structures over time. We demonstrated that our new reference frame optimization outperforms existing local [13] and global [16] optimization methods. In the optimal frame, bifurcation lines are more accurately extracted than with local approximations [33] and they are independent of the integration duration [40]. Further, the separatrices in the optimal frame correspond to the streakline-based topology [40], but can be computed per time slice in the entire domain.

We believe that our work can spur a wealth of follow-up research, for instance on the identification of Hopf and fold bifurcations, and on many other topological elements that we have not studied yet, including saddle connectors, and recirculations. There has been extensive research on the analysis of higher-order topological structures [7,42,53]. We assume that these methods would carry directly into the optimal reference frame, but this is still subject to further research.

ACKNOWLEDGMENTS

REFERENCES

[1] G. Astarita. Objective and generally applicable criteria for flow classification. *Journal of Non-Newtonian Fluid Mechanics*, 6(1):69–76, 1979.

[2] H. Bhatia, V. Pascucci, R. M. Kirby, and P.-T. Bremer. Extracting features from time-dependent vector fields using internal reference frames. *Computer Graphics Forum (Proc. EuroVis)*, 33(3):21–30, 2014.

[3] R. Bujack, S. Dutta, I. Baeza Rojo, D. Zhang, and T. Günther. Objective finite-time saddles and their connection to FTLE. In *Eurographics Conference on Visualization - Short Papers*, 2019.

[4] R. Bujack, M. Hlawitschka, and K. I. Joy. Topology-inspired Galilean invariant vector field analysis. In *IEEE Pacific Visualization Symposium*, pages 72–79, April 2016.

[5] W. de Leeuw and R. van Liere. Collapsing flow topology using area metrics. In *Proceedings of the Conference on Visualization*, VIS '99, pages 349–354, 1999.

[6] R. Drouot and M. Lucius. Approximation du second ordre de la loi de comportement des fluides simples. lois classiques déduites de lintroduction dun nouveau tenseur objectif. *Archiwum Mechaniki Stosowanej*, 28(2):189–198, 1976.

[7] F. Effenberger and D. Weiskopf. Finding and classifying critical points of 2D vector fields: A cell-oriented approach using group theory. *Computing and Visualization in Science*, 13(8):377–396, Dec. 2010.

[8] R. Fuchs, J. Kemmler, B. Schindler, J. Waser, F. Sadlo, H. Hauser, and R. Peikert. Toward a Lagrangian vector field topology. *Computer Graphics Forum*, 29(3):1163–1172, 2010.

[9] T. Germer, M. Otto, R. Peikert, and H. Theisel. Lagrangian coherent structures with guaranteed material separation. In *Computer Graphics Forum*, volume 30, pages 761–770. Wiley Online Library, 2011.

[10] A. Globus, C. Levit, and T. Lasinski. A tool for visualizing the topology of three-dimensional vector fields. In *Proc. IEEE Visualization*, pages 33–40, 1991.

[11] T. Günther, M. Gross, and H. Theisel. Generic objective vortices for flow visualization. *ACM Transactions on Graphics (Proc. SIGGRAPH)*, 36(4):to appear, 2017.

[12] T. Günther, M. Schulze, and H. Theisel. Rotation invariant vortices for flow visualization. *IEEE Transactions on Visualization and Computer Graphics (Proc. IEEE SciVis 2015)*, 22(1):817–826, 2016.

[13] T. Günther and H. Theisel. Hyper-objective vortices. *IEEE Transactions on Visualization and Computer Graphics*, 2018.

[14] T. Günther and H. Theisel. The state of the art in vortex extraction. *Computer Graphics Forum*, 37(6):149–173, 2018.

[15] T. Günther and H. Theisel. Objective vortex corelines of finite-sized objects in fluid flows. *IEEE Transactions on Visualization and Computer Graphics (Proc. IEEE SciVis)*, 25(1), Jan 2019.

[16] M. Hadwiger, M. Mlejnek, T. Theul, and P. Rautek. Time-dependent flow seen through approximate observer killing fields. *IEEE Transactions on Visualization and Computer Graphics*, 25(1):1257–1266, Jan 2019.

[17] G. Haller. Finding finite-time invariant manifolds in two-dimensional velocity fields. *Chaos: An Interdisciplinary Journal of Nonlinear Science*, 10(1):99–108, 2000.

[18] G. Haller. Distinguished material surfaces and coherent structures in three-dimensional fluid flows. *Physica D: Nonlinear Phenomena*, 149(4):248–277, Mar. 2001.

[19] G. Haller. An objective definition of a vortex. *Journal of Fluid Mechanics*, 525:1–26, 2005.

[20] G. Haller. A variational theory of hyperbolic Lagrangian coherent structures. *Physica D: Nonlinear Phenomena*, 240(7):574–598, 2011.

[21] G. Haller. Lagrangian coherent structures. *Annual Review of Fluid Mechanics*, 47:137–162, 2015.

[22] G. Haller, A. Hadjighasem, M. Farazmand, and F. Huhn. Defining coherent vortices objectively from the vorticity. *Journal of Fluid Mechanics*, 795:136–173, 2016.

[23] C. Heine, H. Leitte, M. Hlawitschka, F. Iuricich, L. De Floriani, G. Scheuermann, H. Hagen, and C. Garth. A survey of topology-based methods in visualization. *Computer Graphics Forum*, 35(3):643–667, 2016.

[24] R. Heinze, A. Dipankar, C. C. Henken, C. Moseley, O. Sourdeval, et al. Large-eddy simulations over germany using ICON: a comprehensive evaluation. *Quarterly Journal of the Royal Meteorological Society*, 143(702):69–100, 2017.

[25] J. L. Helman and L. Hesselink. Representation and display of vector field topology in fluid flow data sets. *Computer*, 22(8):27–36, 1989.

[26] J. L. Helman and L. Hesselink. Visualizing vector field topology in fluid flows. *IEEE Computer Graphics and Applications*, 11:36–46, May 1991.

[27] J. Kasten, J. Reininghaus, H. I., H.-C. Hege, B. R. Noack, G. Daviller, and M. Morzynski. Acceleration feature points of unsteady shear flows. *Archives of Mechanics*, 68(1):to appear, 2016.

[28] B. Kim and T. Günther. Robust reference frame extraction from unsteady 2D vector fields with convolutional neural networks. *Computer Graphics Forum (Proc. EuroVis)*, 38(3), 2019.

[29] A. Kuhn, C. Rössl, T. Weinkauf, and H. Theisel. A benchmark for evaluating FTLE computations. In *Proceedings of 5th IEEE Pacific Visualization Symposium (PacificVis 2012)*, pages 121–128, Songdo, Korea, 2012.

[30] R. Laramee, H. Hauser, L. Zhao, and F. Post. Topology-based flow visualization, the state of the art. In *Topology-based Methods in Visualization*, Mathematics and Visualization, pages 1–19. Springer Berlin Heidelberg, 2007.

[31] J.-M. Liu, Y.-S. Gao, Y.-Q. Wang, and C. Liu. Objective omega vortex identification method. *Journal of Hydrodynamics*, Mar 2019.

[32] H. J. Lugt. The dilemma of defining a vortex. In *Recent developments in theoretical and experimental fluid mechanics*, pages 309–321. Springer, 1979.

[33] G. M. Machado, S. Boblest, T. Ertl, and F. Sadlo. Space-time bifurcation lines for extraction of 2D Lagrangian coherent structures. *Computer Graphics Forum (Proc. EuroVis)*, 35(3):to appear, 2016.

[34] R. Peikert and M. Roth. The "parallel vectors" operator – a vector field visualization primitive. In *Proc. IEEE Visualization*, pages 263–270, 1999.

[35] A. E. Perry and M. S. Chong. Topology of flow patterns in vortex motions and turbulence. *Applied Scientific Research*, 53(3):357–374, 1994.

[36] A. Pobitzer, R. Peikert, R. Fuchs, B. Schindler, A. Kuhn, H. Theisel, K. Matkovic, and H. Hauser. The state of the art in topology-based visualization of unsteady flow. *Computer Graphics Forum*, 30(6):1789–1811, 2011.

[37] S. Popinet. Gerris flow solver. `http://gfs.sourceforge.net/wiki/index.php`, 2013.

[38] S. K. Robinson. Coherent motions in the turbulent boundary layer. *Annual Review of Fluid Mechanics*, 23(1):601–639, 1991.

[39] M. Roth and R. Peikert. A higher-order method for finding vortex core lines. In *Proc. IEEE Visualization*, pages 143–150, 1998.

[40] F. Sadlo and D. Weiskopf. Time-dependent 2-D vector field topology: An approach inspired by Lagrangian coherent structures. *Computer Graphics Forum*, 29(1):88–100, 2010.

[41] J. Sahner. *Extraction of Vortex Structures in 3D Flow Fields*. PhD thesis, University of Magdeburg, Germany, April 2009.

[42] G. Scheuermann, H. Kruger, M. Menzel, and A. Rockwood. Visualizing nonlinear vector field topology. *IEEE Transactions on Visualization and Computer Graphics*, 4(2):109–116, 1998.

[43] G. Scheuermann and X. Tricoche. Topological methods for flow. *The Visualization Handbook*, page 341, 2005.

[44] A. A. Shabana. *Computational continuum mechanics*. John Wiley & Sons, 2018.

[45] S. C. Shadden. Lagrangian coherent structures. http://mmae.iit.edu/shadden/LCS-tutorial/, 2005.

[46] S. C. Shadden, F. Lekien, and J. E. Marsden. Definition and properties of Lagrangian coherent structures from finite-time Lyapunov exponents in two-dimensional aperiodic flows. *Physica D: Nonlinear Phenomena*, 212(3-4):271–304, 2005.

[47] D. Sujudi and R. Haimes. Identification of swirling flow in 3D vector fields. Technical report, Departement of Aeronautics and Astronautics, MIT, 1995. AIAA Paper 95-1715.

[48] M. Tabor and I. Klapper. Stretching and alignment in chaotic and turbulent flows. *Chaos, Solitons & Fractals*, 4(6):1031–1055, 1994.

[49] H. Theisel, J. Sahner, T. Weinkauf, H.-C. Hege, and H.-P. Seidel. Extraction of parallel vector surfaces in 3D time-dependent fields and application to vortex core line tracking. In *Proc. IEEE Visualization*, pages 631–638, 2005.

[50] H. Theisel and H.-P. Seidel. Feature flow fields. In *Proc. Symposium on Data Visualisation*, pages 141–148, 2003.

[51] H. Theisel, T. Weinkauf, H.-C. Hege, and H.-P. Seidel. Grid-independent detection of closed stream lines in 2D vector fields. In *Vision, Modeling and Visualization*, volume 4, pages 421–428, 2004.

[52] H. Theisel, T. Weinkauf, H.-C. Hege, and H.-P. Seidel. Stream line and path line oriented topology for 2d time-dependent vector fields. In *Proceedings of the conference on Visualization'04*, pages 321–328. IEEE Computer Society, 2004.

[53] X. Tricoche, G. Scheuermann, and H. Hagen. A topology simplification method for 2D vector fields. In *Proc. Visualization*, pages 359–366, Oct 2000.

[54] M. Üffinger, F. Sadlo, and T. Ertl. A time-dependent vector field topology based on streak surfaces. *IEEE TVCG*, 19(3):379–392, 2013.

[55] G. H. Vatistas, V. Kozel, and W. Mih. A simpler model for concentrated vortices. *Experiments in Fluids*, 11(1):73–76, 1991.

[56] T. Weinkauf. *Extraction of Topological Structures in 2D and 3D Vector Fields*. PhD thesis, University Magdeburg, 2008.

[57] T. Weinkauf, J. Sahner, H. Theisel, and H.-C. Hege. Cores of swirling particle motion in unsteady flows. *IEEE Transactions on Visualization and Computer Graphics (Proc. Visualization)*, 13(6):1759–1766, 2007.

[58] T. Weinkauf, H. Theisel, A. V. Gelder, and A. Pang. Stable feature flow fields. *IEEE Transactions on Visualization and Computer Graphics*, 17(6):770–780, 2011.

[59] T. Weinkauf, H. Theisel, H.-C. Hege, and H.-P. Seidel. Boundary switch connectors for topological visualization of complex 3D vector fields. In *VisSym*, pages 183–192, 2004.

[60] A. Wiebel. Feature detection in vector fields using the Helmholtz-Hodge decomposition. Diploma thesis, Univ. Kaiserslautern, 2004.

[61] A. Wiebel, R. Chan, C. Wolf, A. Robitzki, A. Stevens, and G. Scheuermann. Topological flow structures in a mathematical model for rotation-mediated cell aggregation. *Topological Data Analysis and Visualization: Theory, Algorithms and Applications*, pages 1–12, 2009.

[62] A. Wiebel, C. Garth, and G. Scheuermann. Computation of localized flow for steady and unsteady vector fields and its applications. *IEEE Transactions on Visualization and Computer Graphics*, 13(4):641, 2007.

[63] A. Wiebel, X. Tricoche, D. Schneider, H. Janicke, and G. Scheuermann. Generalized streak lines: Analysis and visualization of boundary induced vortices. *IEEE Trans. on Visualization and Computer Graphics*, 13(6):1735–1742, 2007.

[64] T. Wilde, C. Rssi, and H. Theisel. Recirculation surfaces for flow visualization. *IEEE Transactions on Visualization and Computer Graphics (Proc. IEEE Scientific Visualization)*, 25(1):946–955, Jan 2019.

[65] T. Wischgoll and G. Scheuermann. Detection and visualization of closed streamlines in planar flows. *IEEE Transactions on Visualization and Computer Graphics*, 7(2):165–172, 2001.